

Data assimilation for networks of coupled oscillators: Inferring unknown model parameters from partial observations

Lauren D Smith¹ and Georg A Gottwald²

¹Department of Mathematics, The University of Auckland, Auckland 1142,
New Zealand

²School of Mathematics and Statistics, The University of Sydney, Sydney,
NSW 2006, Australia

October 24, 2024

Abstract

Inferring the state and unknown parameters of a network of coupled oscillators, such as neurons in the brain, is of utmost importance. This task is made harder when only partial and noisy observations are available, which is a typical scenario in realistic high-dimensional systems. The general task of inference falls under data assimilation, and a commonly used assimilation method is the Ensemble Kalman Filter. Employing network-specific localization of the forecast covariance, an Ensemble Kalman Filter with state space augmentation is shown to yield highly accurate estimates of both the oscillator phases and unknown model parameters in the case where only a subset of oscillator phases are observed. In contrast, standard data assimilation methods yield poor results. We demonstrate the effectiveness of our approach for Kuramoto oscillators and for networks of theta neurons, using a variety of network topologies.

1 Introduction

Many natural phenomena and engineering applications can be described as networks of coupled oscillators, for example, the firing of neurons in the brain [1–3] and the dynamics of power grids [4–7]. However, mathematical models for these systems are often incomplete, with unknown parameters and simplifying physical assumptions. Scientists are now seeking data-driven methods to improve estimates of the dynamic state of these systems using observational data, and to simultaneously estimate unknown parameters.

A pertinent question is: Can one accurately estimate all the oscillators’ phases as well as unknown model parameters if only a subset of the oscillator phases are observed? For example, in a power grid, we may be able to observe all the power stations, but none of the consumers. The framework of data assimilation (DA) provides a unifying framework that estimates a system’s state and unknown parameters by optimally combining two uncertain pieces of information – the output of our imperfect model (the model forecast) and noisy partial observations of the system at discrete time intervals.

We focus specifically on the Ensemble Kalman Filter (EnKF) [8–14] as a DA method. Although the framework of Kalman filters can strictly only be applied to linear systems, the EnKF has been successfully used in numerous non-linear settings [15], in particular, weather forecasting [8–14]. To date, there have been only a few applications of DA to the broad class of non-linear systems that model coupled oscillators on complex networks [16, 17]. These applications, however, assume that all nodes are observed. Indeed, we find that the standard EnKF performs poorly for networks of coupled oscillators unless all nodes are observed or very large ensembles are used. Localization has been recognized as an essential component for successful performance of EnKFs [18, 19]. In order to employ localization, a notion of distance is required. In applications involving partial differential equations on spatial domains, for example in weather forecasting, the Euclidean distance is appropriate and localization has shown to be highly efficient in mitigating detrimental small ensemble size effects. It is less clear how best to incorporate “distance” and localization for dynamics on networks. We introduce a novel localization method, specific to dynamics on networks, which renders the EnKF highly effective at estimating both oscillator phases and unknown model parameters, even when a small ensemble is used and only a fraction of the phases are observed. This sets DA apart from other data-driven parameter estimation methods that require all oscillator phases to be observed [20–23]. We demonstrate our method for the Kuramoto model [24–31] which captures the synchronization phenomena observed in many coupled oscillator systems, and for networks of theta neurons [32–35] which model neural dynamics of the brain.

The article is organized as follows. In Section 2 we introduce the Kuramoto model and the theta neuron model, which are the models we use to test the efficacy of our DA methods. In Section 3 we give details of the Ensemble Kalman Filter and our novel network-specific localization procedure. In Section 4 we apply our DA methods to the Kuramoto model (Section 4.1) and to the theta neuron model (Section 4.2), showing that the EnKF with network specific localization provides a great improvement over the standard EnKF. In Section 5 we summarize our results.

2 Models and their dynamics

We consider two prototypical examples of coupled phase oscillators; the Kuramoto model and networks of theta neurons. Here we describe the details of the models and their dynamics.

2.1 The Kuramoto model

Due to its ability to describe many real-world synchronization phenomena and its analytical tractability, the dynamics of the Kuramoto model [24] has been widely studied [25–31]. For N oscillators, the dynamics of the i -th oscillator is

$$\dot{\phi}_i = \omega_i + \frac{\kappa}{N} \sum_{j=1}^N A_{ij} \sin(\phi_j - \phi_i), \quad (1)$$

where ω_i is the oscillator’s natural frequency, κ is the coupling strength and A is the network adjacency matrix, such that $A_{ij} = 1$ if nodes i and j are connected and $A_{ij} = 0$ otherwise.

By moving to a rotating reference frame, we may assume without loss of generality that the mean of the natural frequencies is zero, and in the rotating reference frame a synchronized state appears as a stationary state with all phases approximately equal. An example of this is shown in Fig. 1, such that initially random phases rapidly align and synchronize. In this case

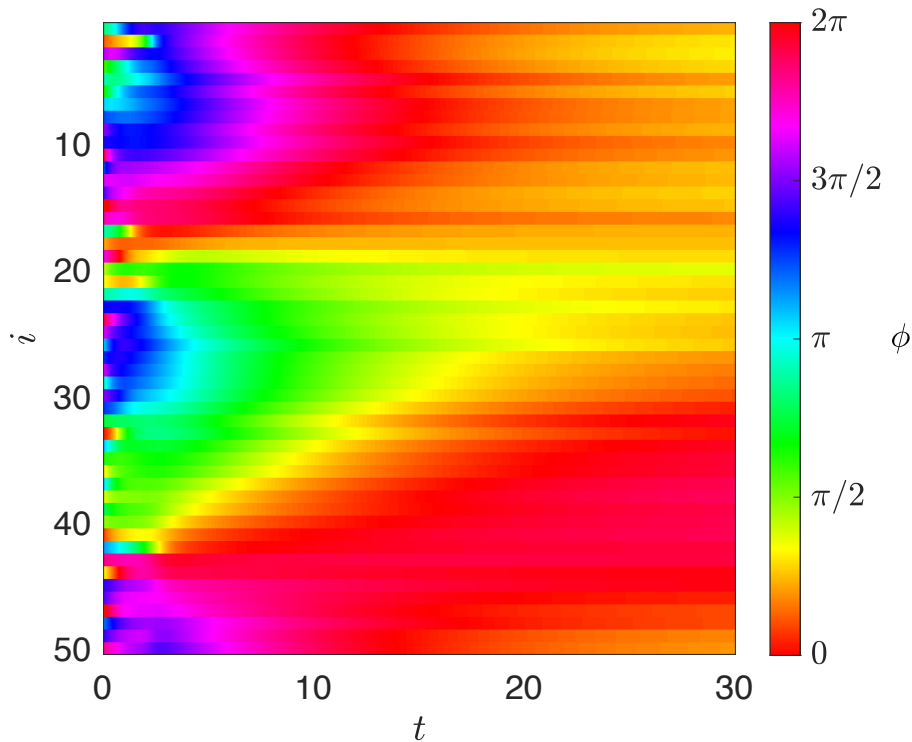


Figure 1: Time evolution of the $N = 50$ phases ϕ_i of the Kuramoto model (1) showing convergence to a synchronized state. The Kuramoto model parameters are $\kappa = 27$ and $\omega_i \sim \mathcal{N}(0, 0.1)$, with a ring network topology A with coupling radius $r = 3$, where each node is connected to its $2r$ nearest neighbors.

a ring network topology is used, but the same synchronization phenomenon is universal to all network topologies for sufficiently large coupling strengths κ .

We will consider in Section 4.1 the challenge to accurately estimate all the phases ϕ_i and all the natural frequencies ω_i , given only noisy observations of a subset of the phases and none of the frequencies.

2.2 Networks of theta neurons

The theta neuron model is a canonical toy model for neural activity in the brain. The model uses a SNIC-bifurcation normal form to model integrate-and-fire neurons [32–35]. In a network of N theta neurons, the dynamics of the i -th neuron is given by

$$\dot{\phi}_i = 1 - \cos \phi_i + (1 + \cos \phi_i) (\zeta_i + \kappa I_i), \quad (2)$$

where κ is a coupling strength, ζ_i is an intrinsic parameter that represents the neuron’s threshold energy to fire, and I_i is the input from other neurons to neuron i given by

$$I_i = \frac{2\pi}{N} \sum_{j=1}^N B_{ij} P(\phi_j),$$

where $P(\phi) = a(1 - \cos \phi)^2$, with a such that $\int_0^{2\pi} P(\phi) d\phi = 2\pi$, and $B_{ij} \in \mathbb{R}$ is the connectivity between nodes i and j , which may be negative for inhibitive coupling. When a neuron receives sufficient input from its neighbors, it overcomes its threshold energy and fires, completing a revolution of the unit circle. This firing provides input to the neuron’s neighbors which in

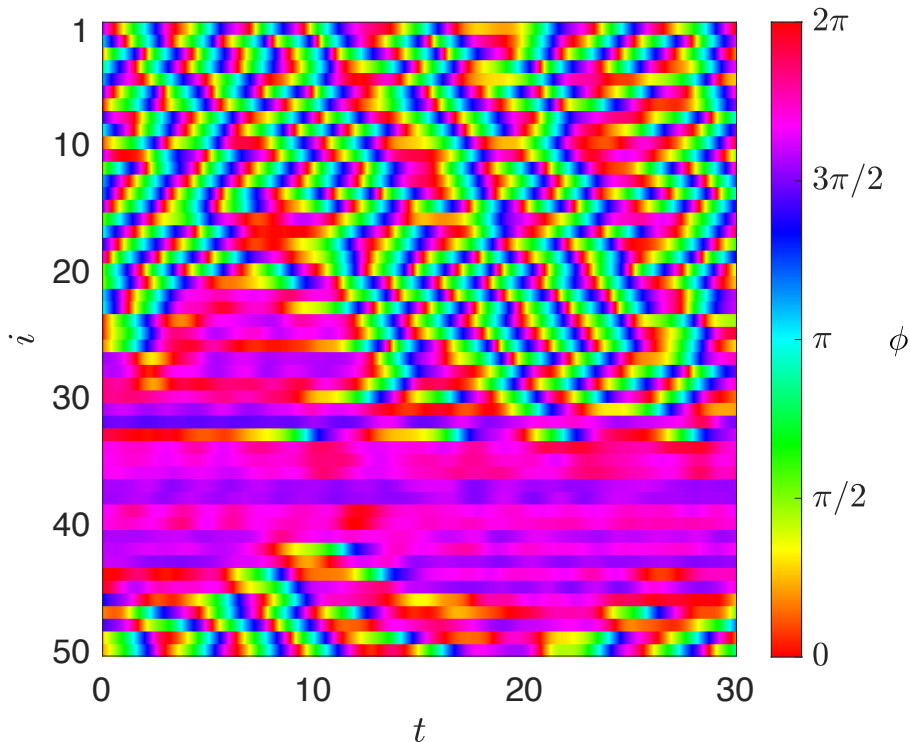


Figure 2: Time evolution of the $N = 50$ phases ϕ_i of the theta neuron model (2) showing a bump state. The theta neuron model parameters are $\kappa = 2$ and $\zeta_i \sim \mathcal{N}(-0.4, 0.1)$, with connectivity matrix B described in Section 4.2.

turn may cause them to fire. In such a network, many irregular and sustained firing patterns are possible depending on the model parameters and the initial condition. An example of a “bump state” is shown in Fig. 2, with a region of neurons that fire approximately periodically and another region of neurons that do not fire at all. Such bump states occur when there is short-range positive coupling, and long-range inhibitive coupling [36]. Bump states are thought to be connected to short term memory [37].

We will consider in Section 4.2 the challenge to accurately estimate all the phases ϕ_i and all the intrinsic firing parameters ζ_i , given only noisy observations of a subset of the phases and none of the firing parameters ζ_i .

3 Ensemble Kalman Filter (EnKF) for coupled oscillators on networks

To solve the inference problem of estimating the state of a system and unknown parameters of the underlying model in the case that only some of the state variables are observed we employ the Ensemble Kalman Filter (EnKF). Kalman filters estimate the posterior distribution of the state given a model forecast and noisy observations. At each discrete time-step t_n , the EnKF optimally combines a forecast ensemble X_n^f obtained by independently simulating the full non-linear model from a previous DA step, and noisy observations Y_n to yield an improved ‘analysis’ ensemble.

We describe here in detail the implementation of the EnKF for networks of coupled oscillators. We note that while many aspects of the method can be traced back to previous studies, changes must be made to accommodate for periodic phase variables that lie on a circle. We recall that the states are labelled as $\phi \in \mathbb{R}^N$ and the parameters are $\mathbf{p} \in \mathbb{R}^N$ (here \mathbf{p} represents

either the natural frequencies ω_i of the Kuramoto model (1) or the intrinsic parameters ζ_i of the theta neuron model (2)). To incorporate parameter estimation into an EnKF analysis step, an augmented state space $X = (\phi, \mathbf{p}) \in \mathbb{R}^{2N}$ is used [11, 12, 38].

In a Kalman filter, a Gaussian approximation of the posterior distribution is performed and one seeks expressions for the mean X^a and the covariance matrix P^a of the posterior. We present here the algorithmic details to compute X^a and P^a . For more details and derivations the reader is referred to [8–14]. The analysis X_n^a at time t_n is the optimal estimate of the state given a forecast X_n^f and an observation Y_n . Treating X_n^f and X_n^a , $n \geq 0$ as random variables and assuming a Gaussian distribution for X_{n+1}^f , the analysis step for the mean \bar{X}_n^a is given by

$$\bar{X}_n^a = \bar{X}_n^f - K_n(H\bar{X}_n^f - Y_n), \quad (3)$$

where the observation matrix $H = (H_\phi \mathbf{0}) \in \mathbb{R}^{N_{\text{obs}} \times 2N}$ projects from the (augmented) state space to the observation space. Here N_{obs} denotes the number of observed state variables. If, for example, only the first phase ϕ_1 is observed, i.e. $N_{\text{obs}} = 1$, then $H = (1, 0, \dots, 0) \in \mathbb{R}^{1 \times 2N}$. The Kalman gain matrix K_n is given by

$$K_n = P_n^f H^T (H P_n^f H^T + R)^{-1} \quad (4)$$

with forecast covariance matrix P_n^f and observational error covariance matrix R . We assume a diagonal observational error covariance with $R = \eta^2 I$. The covariance matrix of the analysis is given by

$$P^a = (I - KH)P^f. \quad (5)$$

We employ a stochastic EnKF [11, 13, 39, 40] to implement the Kalman analysis step. Ensemble Kalman filters allow for a dynamically adapted estimation of the forecast covariances P_n^f , and they proved to be advantageous for nonlinear forward models, and for non-Gaussian augmented state variables. Consider an ensemble of states $\mathbf{X} \in \mathbb{R}^{2N \times M}$ consisting of M members $X^{(i)} \in \mathbb{R}^{2N \times 1}$, $i = 1, \dots, M$, that is,

$$\mathbf{X} = [X^{(1)}, X^{(2)}, \dots, X^{(M)}], \quad (6)$$

with empirical mean

$$\bar{X} = \frac{1}{M} \sum_{k=1}^M X^{(k)}. \quad (7)$$

The associated matrix of ensemble deviations is given by

$$\hat{\mathbf{X}} = [X^{(1)} - \bar{X}, X^{(2)} - \bar{X}, \dots, X^{(M)} - \bar{X}]. \quad (8)$$

Note that for a 2π -periodic phase variable $X_j = \phi_j$, the phase-mean $\bar{\phi}_j$ of the ensemble $\phi_j^{(k)}$, $k = 1, \dots, M$, given by

$$\rho e^{i\bar{\phi}_j} = \frac{1}{M} \sum_{k=1}^M e^{i\phi_j^{(k)}}, \quad (9)$$

is used instead of the empirical mean and the ensemble deviations are defined as

$$F\left(\phi_j^{(k)} - \bar{\phi}_j\right), \quad k = 1, \dots, M, \quad (10)$$

where $F(\theta) = \text{mod}(\theta + \pi, 2\pi) - \pi$ ensures that differences are centered at 0 in the interval $[-\pi, \pi)$. Ensembles for the forecast are denoted again by superscript f and those for the analysis by superscript a. In the forecast step the ϕ -component of each ensemble member is propagated

independently using the non-linear forecast model (i.e., either the Kuramoto model (1) or the theta-neuron model (2)), updating the previous analysis ensemble \mathbf{X}_{n-1}^a to the next forecast ensemble \mathbf{X}_n^f . The parameter component \mathbf{p} of each ensemble member is considered constant during the forecast step, i.e. $\dot{\mathbf{p}} = 0$. The forecast covariance matrix P_n^f used in the analysis step (3) is estimated as a Monte-Carlo approximation from the forecast ensemble deviation matrix $\hat{\mathbf{X}}_n^f$ via

$$P_n^f = \frac{1}{M-1} \hat{\mathbf{X}}_n^f (\hat{\mathbf{X}}_n^f)^T \in \mathbb{R}^{2N \times 2N}. \quad (11)$$

To ensure that the analysis ensemble is statistically consistent with the Kalman filter, and, in particular, with the analysis error covariance (5), in the stochastic ensemble Kalman filter [11, 39] observations Y_n receive a stochastic perturbation $\boldsymbol{\eta}_n^{(i)} \in \mathbb{R}^{N_{\text{obs}} \times 1}$, $i = 1, \dots, M$, drawn independently from the Gaussian observational noise distribution $\mathcal{N}(\mathbf{0}, R)$. The associated ensemble of perturbed observations $\tilde{\mathbf{Z}}_n \in \mathbb{R}^{N_{\text{obs}} \times M}$ is given by

$$\tilde{\mathbf{Z}}_n = [Y_n - \boldsymbol{\eta}_n^{(1)}, Y_n - \boldsymbol{\eta}_n^{(2)}, \dots, Y_n - \boldsymbol{\eta}_n^{(M)}]. \quad (12)$$

The EnKF analysis update step is then given by

$$\mathbf{X}_n^a = \mathbf{X}_n^f - K_n \Delta \mathbf{I}_n, \quad (13)$$

with the Kalman gain defined by (4) using (11) and the stochastic innovation

$$\Delta \mathbf{I}_n = H \mathbf{X}_n^f - \tilde{\mathbf{Z}}_n. \quad (14)$$

In finite ensembles members may align, on short time scales, with the most unstable direction leading to an ensemble collapse in which many ensemble members become indistinguishable. This leads to filter divergence in which the filter believes its own forecast since P^f is small, and the forecast is not corrected by new incoming observations. To mitigate against such finite ensemble size effects we employ, as is typically done, covariance inflation with $P_n^f \rightarrow \delta P_n^f$ with $\delta = 1.001$ [41]. This multiplicative inflation does not effect the ensemble mean but increases the forecast error covariance.

3.1 Splitting the analysis step into phase and parameter components

For our ensemble $\mathbf{X} = [X^{(1)}, X^{(2)}, \dots, X^{(M)}] \in \mathbb{R}^{2N \times M}$, we can write each ensemble member in the form

$$X^{(j)} = \begin{pmatrix} \boldsymbol{\phi}^{(j)} \\ \mathbf{p}^{(j)} \end{pmatrix} \in \mathbb{R}^{2N \times 1}, \quad (15)$$

such that $\boldsymbol{\phi}^{(j)} = (\phi_1^{(j)}, \dots, \phi_N^{(j)})^T \in \mathbb{R}^{N \times 1}$ and $\mathbf{p}^{(j)} = (p_1^{(j)}, \dots, p_N^{(j)})^T \in \mathbb{R}^{N \times 1}$. Following (8)-(10) we can define ensemble deviations for the phases and parameters separately, i.e.,

$$\hat{\boldsymbol{\Phi}} = [F(\boldsymbol{\phi}^{(1)} - \bar{\boldsymbol{\phi}}), \dots, F(\boldsymbol{\phi}^{(M)} - \bar{\boldsymbol{\phi}})], \quad \hat{\boldsymbol{\Pi}} = [\mathbf{p}^{(1)} - \bar{\mathbf{p}}, \dots, \mathbf{p}^{(M)} - \bar{\mathbf{p}}], \quad (16)$$

where $\bar{\boldsymbol{\phi}}$ is the vector of phase means (9) and F is as in (10). Therefore, the ensemble deviations (8) are given by

$$\hat{\mathbf{X}} = \begin{pmatrix} \hat{\boldsymbol{\Phi}} \\ \hat{\boldsymbol{\Pi}} \end{pmatrix}. \quad (17)$$

From (11), it follows that the forecast covariance matrix is given by

$$P_n^f = \frac{1}{M-1} \begin{pmatrix} \hat{\boldsymbol{\Phi}}_n^f (\hat{\boldsymbol{\Phi}}_n^f)^T & \hat{\boldsymbol{\Phi}}_n^f (\hat{\boldsymbol{\Pi}}_n^f)^T \\ \hat{\boldsymbol{\Pi}}_n^f (\hat{\boldsymbol{\Phi}}_n^f)^T & \hat{\boldsymbol{\Pi}}_n^f (\hat{\boldsymbol{\Pi}}_n^f)^T \end{pmatrix} = \begin{pmatrix} P_{\boldsymbol{\phi}\boldsymbol{\phi}}^f & P_{\boldsymbol{\phi}\mathbf{p}}^f \\ P_{\mathbf{p}\boldsymbol{\phi}}^f & P_{\mathbf{p}\mathbf{p}}^f \end{pmatrix}, \quad (18)$$

such that $P_{\phi\phi}^f$ is the covariance matrix of the phases only, $P_{\phi p}^f$ is the covariance between the phases and parameters, etc.

Since we only observe the phases ϕ , we can separate the state and parameter update of the Kalman analysis step (3) as

$$\bar{\phi}_n^a = \bar{\phi}_n^f - P_{\phi\phi}^f H_\phi^T (H_\phi P_{\phi\phi}^f H_\phi^T + R)^{-1} \Delta \mathbf{I}_n \quad (19a)$$

$$\bar{p}_n^a = \bar{p}_n^f - P_{p\phi}^f H_\phi^T (H_\phi P_{\phi\phi}^f H_\phi^T + R)^{-1} \Delta \mathbf{I}_n \quad (19b)$$

with innovation

$$\Delta \mathbf{I}_n := H_\phi \bar{\phi}_n^f - Y_n. \quad (20)$$

We note that the covariance matrix P_{pp}^f , between the parameters and themselves, does not enter this equation.

3.2 Spurious correlations and localization

A source of error in ensemble-based methods arises due to spurious correlations caused by the finite size of the ensemble. If two variables are not correlated, the Monte-Carlo approximation of the covariance yields entries of $\mathcal{O}(1/\sqrt{M})$ compared to the true entry which is 0. One could reduce the effect of spurious correlations by using a very large ensemble size M , but that is computationally prohibitive for high-dimensional systems. An alternative approach is so-called ‘‘localization’’, whereby topological information is used to predetermine and suppress spurious correlations [18], which allows for a smaller ensemble to be used. For example, in weather forecasting, correlations are deemed spurious if the grid-points are geographically distant. It is less clear how to best incorporate localization for dynamics on networks.

We use the Kuramoto model (1) as an illustrative example of spurious correlations, which guides the appropriate form of localization that should be performed. For illustrative purposes we assume that all phase variables ϕ_j are observed at each time step, and that the oscillators are arranged in a ring network topology with coupling radius $r = 3$, where each node is connected to its $2r$ nearest neighbors.

To demonstrate spurious correlations, we normalize the covariance matrices P_n^f at each DA step to obtain correlation matrices Q_n . We generate noisy observations Y_n by adding Gaussian noise with covariance $R = \eta^2 I$ (here $\eta = 0.02$) to simulated trajectories of the Kuramoto model (1). Fig. 3(a,b) shows the averaged correlation matrix Q , for a large ensemble $M = 100(2N + 1) = 10,100$ and a small ensemble $M = 2N + 1 = 101^1$. For the large ensemble, correlations decay rapidly away from the leading diagonal in each sub-block (Fig. 3(a)), reflecting the underlying ring topology. For the small ensemble, however, there are large spurious correlations far from the diagonal (Fig. 3(b)), wrongly suggesting connections between poorly connected nodes. Moreover, the information about the network topology is completely lost in the ϕ - ω correlations $P_{\phi p}^f$, which are crucial for estimating the parameters ω_i (cf. (19b)). To suppress these spurious correlations, and allow for smaller ensembles to be used, localization is required, where at each DA step the covariance matrix P_n^f is replaced by

$$\tilde{P}_n^f = \mathcal{L} \circ P_n^f,$$

where \circ denotes the Schur (elementwise) product, and \mathcal{L} is the localization matrix. Standard localization functions, such as Gaspari-Cohn localization [18, 42], are not suitable for networks, because they rely on Euclidean geometries. We discuss this in detail in Section 3.4. Instead we require \mathcal{L} to have the following properties:

¹Since the augmented state space is $2N$ -dimensional, the minimum ensemble size to ensure a full rank covariance matrix is $M = 2N + 1$.

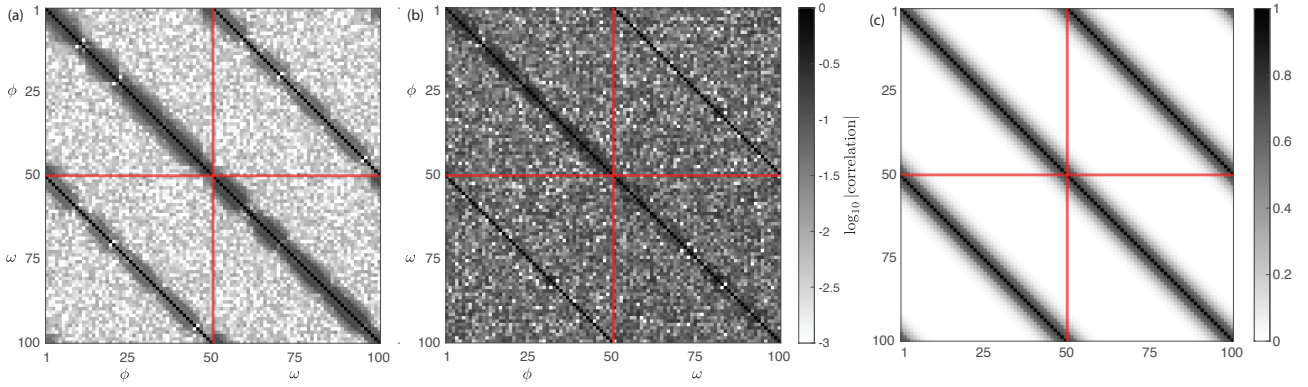


Figure 3: (a) Average correlation matrix Q for a large ensemble ($M = 10100$), and (b) for a small ensemble ($M = 101$), obtained by applying the standard EnKF to the Kuramoto model (1). The augmented state space is $(\phi_{1,\dots,50}, \omega_{1,\dots,50})$, hence the block matrix substructure (indicated by red lines) in Q with ϕ - ϕ correlations, ϕ - ω correlations, ω - ϕ correlations and ω - ω correlations. The Kuramoto model parameters are as in Fig. 1. (c) The localization matrix \mathcal{L} (23) for the associated ring topology using $\lambda = 0.46$ as determined in Section 3.3.

- \mathcal{L} encodes the network connectivity, i.e., \mathcal{L}_{ij} is large if nodes i and j are well connected, and small otherwise,
- \mathcal{L} is a correlation matrix, i.e., positive semi-definite and $\mathcal{L}_{ii} = 1$.

Consider the (symmetric positive semi-definite matrix) covariance matrix, $\mathcal{E} = \exp(\lambda A)$, where λ is a tunable parameter and A is the network adjacency matrix (assumed to be symmetric). The matrix

$$\mathcal{E} = \exp(\lambda A) = \sum_{n=0}^{\infty} \frac{\lambda^n}{n!} A^n \quad (21)$$

is a weighted sum, with decreasing weights, of powers A^n . The entries $(A^n)_{ij}$ count the number of paths of length n between nodes i and j . Hence, \mathcal{E} encodes the network topology. A correlation matrix L is obtained by normalizing \mathcal{E} according to

$$L = (\text{diag}(\mathcal{E}))^{-\frac{1}{2}} \mathcal{E} (\text{diag}(\mathcal{E}))^{-\frac{1}{2}}. \quad (22)$$

To account for the augmented state space with both phases and frequencies we introduce the block matrix

$$\mathcal{L} = \begin{pmatrix} L & L \\ L & L \end{pmatrix}. \quad (23)$$

An example of \mathcal{L} is shown in Fig. 3(c) for the ring topology with $N = 50$, $r = 3$ and $\lambda = 0.46$. The parameter λ controls the rate of decay for distant nodes and is chosen to suppress spurious correlations. We discuss the appropriate choice of λ and a simple heuristic method for determining λ in Section 3.3.

We will show in Section 4 that introducing this network-specific localization \mathcal{L} significantly improves the prediction and estimation accuracy of the EnKF with partial observations for both the Kuramoto model (1) and networks of theta neurons (2).

3.3 Choosing the localization parameter λ

The parameter λ in the localization matrix L (21), (22) is important for controlling the rate of decay of correlations for distant nodes. The optimal value of λ could be found through numerical

optimization, minimizing the RMS error of the DA algorithm across many simulations. Here we present a cheap heuristic method to choose a value of λ at first for ring network topologies, and then we will generalize the method to random network topologies. Our heuristic is based on the typical decay of correlations that is observed from DA for large ensembles.

3.3.1 Ring network topologies

Considering a ring topology with connectivity radius r , we find that the correlations for large ensembles are negligible beyond a radius of $2r$. That is, for a node j , only the nodes k that have shortest path length from j to k less than or equal to 2 have significant correlations, and all other correlations can be considered spurious. This is shown in Fig. 4, which shows the average correlation as a function of distance from the node, scaled by the connectivity radius r . This data is obtained from the standard EnKF applied to the Kuramoto model with $N = 50$ and with a large ensemble $M = 100(2N + 1)$, as in Fig. 3(a) which shows correlations for $r = 3$. Fig. 4 shows that correlations become spurious beyond a distance of $2r$ ($d/r = 2$). Using this information, considering node $j = 1$, the nodes within a radius of $2r$, and which will have significant correlations are $k = 1, \dots, 2r + 1$ and $k = N - r + 1, \dots, N$, and all other nodes, i.e., $k = 2r + 2, \dots, N - r$ will have spurious correlations. Knowing which correlations we wish to suppress, the next question is how much do we need to suppress them? For this, we choose an $0 < \epsilon < 1$, which will be the upper bound for the entries in L (22) beyond a radius of $2r$ from each node. Here we have chosen $\epsilon = 0.1$. Due to the symmetry of the ring topology, and the fact that $\exp(\lambda A)$ decays away from its diagonal, we require that

$$L_{1,2r+2} = \frac{\mathcal{E}_{1,2r+2}}{\mathcal{E}_{1,1}} \leq \epsilon, \quad (24)$$

where $\mathcal{E} = \exp(\lambda A)$ as in (21). Changing the inequality in (24) to an equality gives an equation that can be solved (numerically) for λ in terms of r and ϵ . This is demonstrated schematically in Fig. 5, where the orange squares are the first spurious correlations, with $L_{ij} = \epsilon$. In particular, in the first row we have $L_{1,2r+2} = \epsilon$.

For a fixed value of ϵ , we find that $1/\lambda$ scales approximately linearly with r , independent of N provided $r \ll N$. This is shown in Fig. 6. Fig. 6(a) shows that for fixed $\epsilon = 0.1$, the value of λ obtained from (24) does not depend on N , provided that $r \ll N$. Fig. 6(b) shows different approximately linear scalings between $1/\lambda$ and r for various values of ϵ (all using $N = 200$). This approximately linear scaling will now be utilized to determine appropriate values of λ for general network topologies.

3.3.2 Complex network topologies

We determine the value of λ to use in the localization matrix (21), (22) for a complex network topology based on a ring topology with equivalent mean degree. Consider a complex network topology with mean degree $\langle k \rangle$. The ring topology with the same mean degree has connectivity radius $r^* = \langle k \rangle / 2$ (ignoring for now that this is likely not an integer). We first find λ^* corresponding to the ring topology with $r = r^*$. If r^* is an integer, we follow the procedure described in the previous section for the ring topology, otherwise, we interpolate to find λ^* . We could linearly interpolate between the two nearest integer values of r , but we can do better by noting that $1/\lambda$ scales approximately linearly with r , as shown in Fig. 6. Thus, we find the fit of the form

$$\frac{1}{\lambda} = mr + c, \quad (25)$$

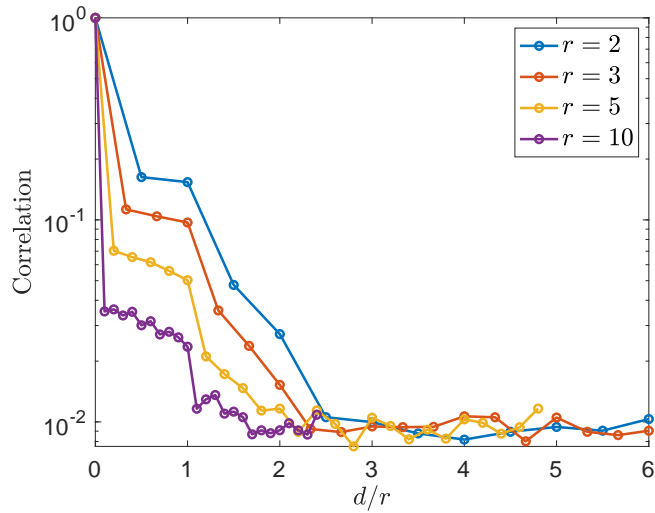


Figure 4: Average forecast correlation (averaging P_k^f over all nodes and all time steps) as a function of distance d from the node, scaled by the coupling radius r , for $r = 2, 3, 5, 10$. All results are obtained from runs of the standard EnKF applied to the Kuramoto model ($N = 50$, $\kappa = 80/r$, $\omega_i \sim \mathcal{N}(0, 0.1)$ with a ring topology), with a large ensemble $M = 100(2N + 1)$. Note that a coupling strength $\kappa = 80/r$ is used to maintain a constant effective coupling strength $\kappa/\langle k \rangle$, where $\langle k \rangle$ is the mean degree.

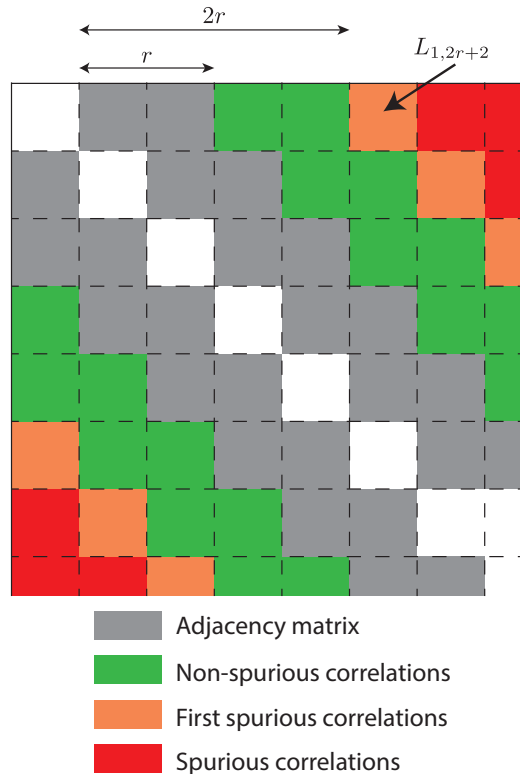


Figure 5: Schematic diagram for the condition (24) that defines λ . Shown is the top right corner of the matrix L , the gray squares indicate the underlying adjacency matrix (here a ring with $r = 2$), the green squares indicate correlations that should not be considered spurious because they are within a distance of $2r$ from the node, and orange/red squares indicate correlations that should be considered spurious because the distance from the node is greater than $2r$. The orange squares are those whose value will be ϵ for λ satisfying (24) with equality, e.g., in the first row $L_{1,2r+2} = \epsilon$.

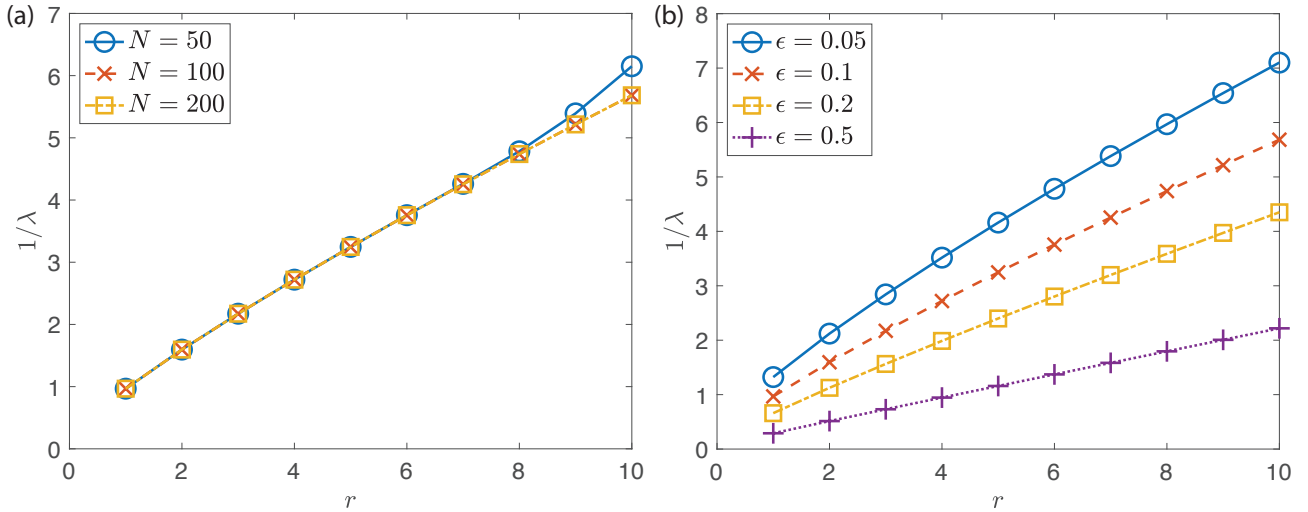


Figure 6: $1/\lambda$ as a function of r for various values of the number of oscillators N and threshold ϵ . In all cases λ is obtained from (24). (a) Fixed $\epsilon = 0.1$, $N = 50, 100, 200$. (b) Fixed $N = 200$, $\epsilon = 0.05, 0.1, 0.2, 0.5$.

passing through $(r_1, 1/\lambda_1)$ and $(r_2, 1/\lambda_2)$, where $r_1 = \lfloor r^* \rfloor \leq r^*$ and $r_2 = \lceil r^* \rceil \geq r^*$ are the two nearest integers to r^* , and λ_1 and λ_2 are the corresponding values of λ obtained from ring topologies. That is,

$$m = \frac{1/\lambda_2 - 1/\lambda_1}{r_2 - r_1}, \quad c = \frac{1}{\lambda_1} - mr_1. \quad (26)$$

The value λ^* is then given by

$$\lambda^* = (mr^* + c)^{-1}. \quad (27)$$

As an example, for an Erdős-Rényi graph $N = 50$ nodes and coupling probability $p = 0.1$, such that each pair of nodes are coupled with probability p , the mean degree is $\langle k \rangle = N(p-1) = 4.5$. The equivalent ring topology has $r^* = 2.45$. The two nearest integers are $r_1 = 2$ and $r_2 = 3$. From the method for ring topologies in the previous section we obtain $\lambda_1 = 0.627$ and $\lambda_2 = 0.460$. Substituting these values into (26), (27) yields $\lambda^* = 0.539$, which is the value of λ used in Section 4.1.3 for random Erdős-Renyi networks.

3.4 Comparison between matrix exponential localization and Gaspari-Cohn localization functions

Localization has been widely employed in applications of the EnKF. However, most applications assume an underlying Euclidean geometry such that the distance between nodes is their Euclidean distance. Based on the assumption of Euclidean geometry, methods have been created to generate localization functions. A widely used method is that of Gaspari & Cohn [42], with the localization function

$$C(z, c) = \begin{cases} -\frac{1}{4} \left(\frac{|z|}{c}\right)^5 + \frac{1}{2} \left(\frac{|z|}{c}\right)^4 + \frac{5}{8} \left(\frac{|z|}{c}\right)^3 - \frac{5}{3} \left(\frac{|z|}{c}\right)^2 + 1, & 0 \leq |z| \leq c, \\ \frac{1}{12} \left(\frac{|z|}{c}\right)^5 - \frac{1}{2} \left(\frac{|z|}{c}\right)^4 + \frac{5}{8} \left(\frac{|z|}{c}\right)^3 + \frac{5}{3} \left(\frac{|z|}{c}\right)^2 - 5 \left(\frac{|z|}{c}\right) + 4 - \frac{2}{3} \left(\frac{|z|}{c}\right)^{-1}, & c \leq |z| \leq 2c, \\ 0, & 2c \leq |z|, \end{cases} \quad (28)$$

where $|z|$ is the Euclidean distance between the nodes and c is a length-scale that controls the decay of correlation. The function C is a 5th-order piecewise rational function with compact

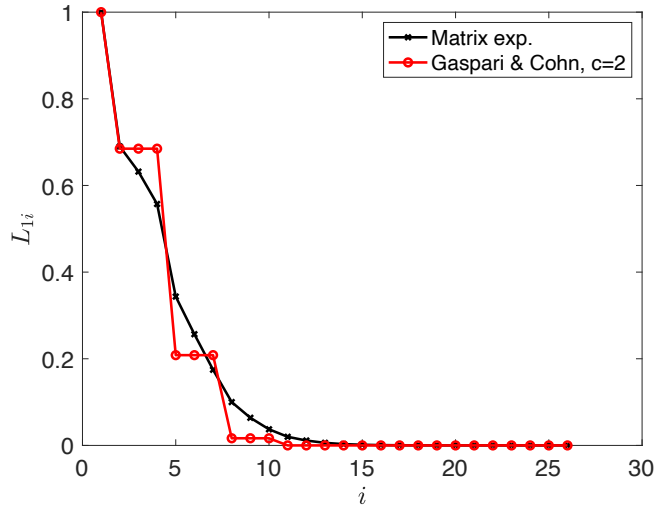


Figure 7: Values L_{1i} from the first row of the matrix exponential correlation matrix shown in Fig. 3(b) using (22) with $\lambda = 0.46$ (black crosses) and values $\tilde{L}_{1i} = C(d(1, i), c)$ using the Gaspari-Cohn function with shortest path length distance (28) with $c = 2$ (red circles). Both use an underlying ring topology with $N = 50$ and $r = 3$.

support. In generating a localization matrix L , one would define $L_{ij} = C(|x_i - x_j|, c)$, where x_i is the position of node i in space, and $|x|$ denotes the Euclidean norm. Note, the proof that C is a correlation function relies on the Euclidean distance being used.

When considering localization on networks, there are many possible definitions of the “distance” between two nodes. Possibly the simplest definition is the shortest path length, that is, the distance $d(i, j)$ between nodes i and j is the length of the shortest path connecting i to j . With this definition, one can, in principle, define the function C from (28), and create a matrix $\tilde{L}_{ij} = C(d(i, j), c)$, where here c is a characteristic length for meaningful correlations. However, this construction does not in general yield a correlation matrix, in particular, the matrix \tilde{L} is not always positive semi-definite. Nevertheless, we can compare the matrix \tilde{L} with L obtained from (22). In Section 3.3 we noted that for ring topologies correlations appear to be spurious for node distances greater than 2, so a choice $c \approx 2$ is natural. Fig. 7 shows the first rows of the respective localization matrices L and \tilde{L} for the ring topology with $N = 50$ and $r = 3$ using the matrix exponential construction (22) (black crosses) compared to the Gaspari-Cohn construction with shortest path length distance (red circles). There is very good agreement between the two constructions.

The similarity between the matrix exponential and the Gaspari-Cohn function with shortest path length distance (28) suggests that the matrix exponential is a good choice for localization. One advantage of the Gaspari-Cohn construction (28) is that the function is compactly supported, resulting in a sparse localization matrix, which in turn reduces the computational cost of data assimilation. One could produce a sparse matrix from the localization matrix L derived from the matrix exponential (22) by setting all entries below a threshold value equal to zero, however, the resulting matrix is not guaranteed to be positive semi-definite. Alternatively, a sparse localization matrix can be obtained by considering a normalization of a matrix of the form

$$B = \sum_{i=0}^n \alpha_i A^i, \quad (29)$$

which is positive definite provided that A is symmetric and $\sum_{i=0}^n \alpha_n \eta^i \geq 0$ for all eigenvalues η of A , and is sparse provided that $n \ll N$. This construction allows for $n + 1$ tunable parameters

α_i . For example, using the matrix exponential as a guide, one could consider the truncation

$$B = \sum_{i=0}^n \frac{\lambda^i}{i!} A^i, \quad (30)$$

for $n \ll N$ and with one parameters λ . However, one would have to check that $\sum_{i=0}^n \frac{\lambda^i}{i!} \eta^i$ is non-negative for all eigenvalues η of A . Consideration of sparse localization matrices of this form is left as an avenue for future work.

4 Results

Each of our data assimilation trials are initialized with an initial ensemble \mathbf{X}_0^a at $t = 0$ with $M = 2N + 1$ members (the minimum required for the covariance matrices to be full rank) and $\phi_0^a \sim \mathcal{N}(\phi_0 + \boldsymbol{\eta}_\phi, \sigma_{\phi,1}^2 I)$, such that ϕ_0 is the true value at $t = 0$ and $\boldsymbol{\eta}_\phi \sim \mathcal{N}(0, \sigma_{\phi,2}^2) \in \mathbb{R}^N$. In essence, $\sigma_{\phi,2}$ controls the perturbations of the ensemble means away from the truth, and $\sigma_{\phi,1}$ controls the spread of the ensemble around the ensemble means. The initial ensemble for the parameters \mathbf{p} has the analogous form $\mathbf{p}_0^a \sim \mathcal{N}(\mathbf{p}_0 + \boldsymbol{\eta}_p, \sigma_{p,1}^2 I)$, such that $\boldsymbol{\eta}_p \sim \mathcal{N}(0, \sigma_{p,2}^2) \in \mathbb{R}^N$. For data assimilation with the Kuramoto model we use $\sigma_{\phi,1}^2 = \sigma_{\phi,2}^2 = 0.25$, and $\sigma_{\omega,1}^2 = \sigma_{\omega,2}^2 = 0.25 \sigma_\omega^2 = 0.025$, where $\sigma_\omega^2 = 0.1$ is the variance of the natural frequency distribution. For data assimilation with the theta neuron network we use $\sigma_{\phi,1}^2 = \sigma_{\phi,2}^2 = 0.04$, and $\sigma_{\zeta,1}^2 = \sigma_{\zeta,2}^2 = 0.04 \sigma_\zeta^2 = 0.004$, where $\sigma_\zeta^2 = 0.1$ is the variance of the intrinsic firing parameter distribution.

To test our data assimilation methods we generate noisy observations Y_n by first simulating the model and then artificially adding noise with prescribed covariance $R = \eta^2 I$ with $\eta = 0.02$. To quantify the skill of the data assimilation procedure, we compute the root mean square (RMS) errors between the true and the DA analysis mean values for the phase variables and the parameters. The RMS error for the phases ϕ_i at time t is

$$E_\phi(t) = \frac{1}{\sqrt{N}} \sqrt{\sum_{i=1}^N (\phi_i(t) - \phi_i^a(t))^2}, \quad (31)$$

where $\phi_i^a(t)$ is the DA estimated value (the analysis mean) and $\phi_i(t)$ is the true value. As in (10), we use the function F to center the phase differences around zero, i.e., in the range $[-\pi, \pi)$. The RMS error for the model parameters, either the natural frequencies ω_i of the Kuramoto model (1) or the intrinsic firing parameters ζ_i of the theta neuron model (2), are computed analogously, and denoted by $E_\omega(t)$ and $E_\zeta(t)$, respectively.

4.1 Data assimilation for the Kuramoto model

We return to the question posed previously: Can DA accurately predict and estimate all of the phase variables ϕ_i and natural frequencies ω_i in the Kuramoto model (1) if only a subset of the phases are observed, with none of the frequencies being observed?

We will first show that our localization scheme significantly improves the accuracy of the EnKF when applied to the Kuramoto model with a ring network topology, for which we have already shown that spurious correlations are significant in Section 3.2. We will then show that our localization scheme also greatly improves DA for random Erdős-Rényi network topologies and scale-free Barabási-Albert network topologies.

In most of our analyses (all except in Section 4.1.2) we initialize the Kuramoto model with a uniformly random initial condition of phases $\phi_i(0)$ on $[0, 2\pi)$. We then observe the

transition of the system from an initially incoherent state to a synchronized state for sufficiently large coupling strength κ . Synchronization presents a challenge for all data-driven methods. In a fully synchronized state, phases co-rotate at a uniform frequency, which is effectively a stationary state in a co-rotating reference frame. Once synchronization occurs, the observations progressively decrease in value, since they yield little new information. In Section 4.1.2 we discuss DA applied to cases with an initially synchronized state. We show that DA is still able to make improvements on the estimates of the phases ϕ_i and natural frequencies ω_i , but the gain in accuracy is less than that obtained from observing the transient which carries more dynamic information.

4.1.1 Ring network topology

As in Section 3.2, we consider a ring network topology with $N = 50$ nodes, such that the nodes are arranged on a circle, and each node is connected to its $2r$ nearest neighbors (here $r = 3$). For our DA process, we consider the case where only 35 out of 50 phases are observed. The observed set of nodes is chosen randomly. Fig. 8(a) shows the RMS errors between the true and the DA estimated values for the phases ϕ_i (dashed) and natural frequencies ω_i (solid), using both the standard (blue) and localized (red) EnKF. Localization greatly reduces the error in both the ϕ_i and ω_i compared to the standard EnKF, with almost 10 times less error in each. The relative errors at time $t = 30$ are shown in Fig. 8(b,c) for each of the ϕ_i and each of the ω_i , respectively. It is again seen that localization (red circles) greatly reduces the error compared to the standard EnKF (blue triangles). As expected, for both methods errors are smaller for nodes whose phase is observed (filled circles/triangles) than for nodes whose phase is unobserved (open circles/triangles). Recall that none of the frequencies ω_i are observed. As expected, errors are largest in regions with a large number of unobserved nodes, e.g., for $i \in [20, 40]$.

As expected, the estimation accuracy increases with the fraction of observed phases. Localization amplifies this effect, and allows for a much smaller set of observed phases to achieve the same estimation accuracy compared to the standard EnKF. We show this using a ring topology and investigate the effect of changing the number of observed phases. To simplify the analysis, we do not choose observed phases at random, but rather require that they are evenly distributed, e.g. every fourth node in the ring is observed/unobserved. For each fraction of observed phases we perform each DA method for 100 random realizations (randomized initial phases, natural frequencies, observation errors and initial ensemble) and take the median over the realizations of the RMS errors of the phases ϕ_i and frequencies ω_i . We consider $N = 60$ which allows more data points for evenly distributed observed/unobserved nodes. The median RMS errors in ϕ (dashed) and ω (solid) are shown in Fig. 9 for different fractions of observed phases, for both the standard EnKF (blue) and the EnKF with network-specific localization (red). We see again a significant decrease in the RMS error when localization is employed. The trends for both the standard EnKF and localized EnKF are similar, with sharp decreases in the error of the phases ϕ_i for fractions of observed phases close to both 0 and 1, and with less decrease in error for fractions of observed phases close to 50%, where there appears to be a point of inflection. For the error in the frequencies ω_i , the localized EnKF shows an initially steady decrease in the error as the fraction of observed phases increases, with significant gains in accuracy for fractions of observed nodes above 50%.

4.1.2 Observations from a fully synchronized state

As in the previous section, we consider the Kuramoto model (1) with a ring network topology with $r = 3$, but instead of a uniformly random initial condition for the phases, we begin with

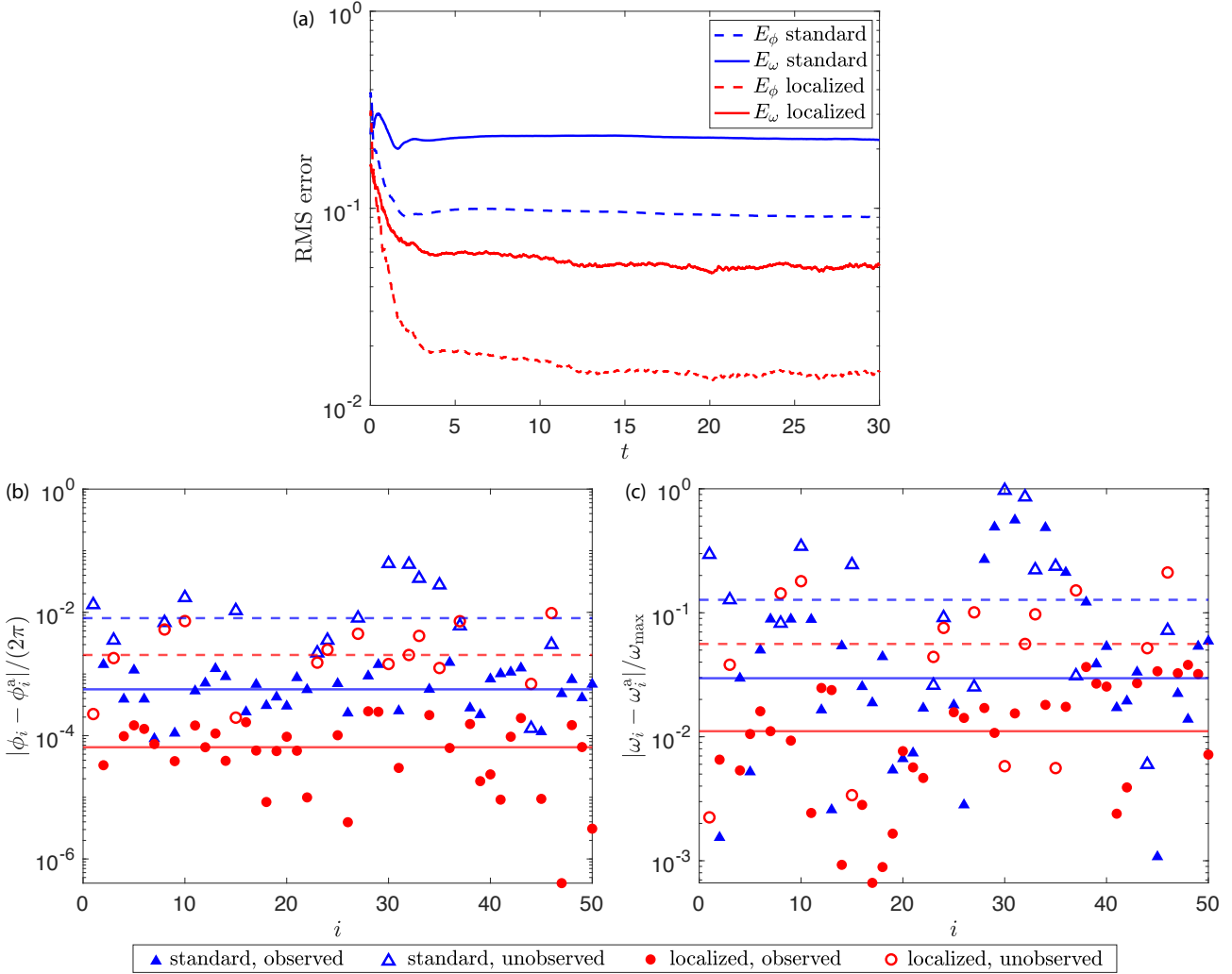


Figure 8: (a) RMS errors in ϕ (dashed) and ω (solid) for DA applied to the Kuramoto model (1) with 35 out of $N = 50$ phases observed. Results are shown for the standard (blue) and localized ((23) using $\lambda = 0.46$) (red) EnKF. (b), (c) Relative errors in ϕ_i and ω_i , respectively, at final time $t = 30$ for the standard (blue triangles) and localized (red circles) EnKF. Filled symbols indicate nodes whose phase (but not frequency) is being observed, and open symbols indicate nodes whose phase and frequency are unobserved. Median errors are shown as horizontal lines; blue for standard, red for localized, solid for observed, dashed for unobserved. The Kuramoto model parameters are as in Fig. 1.

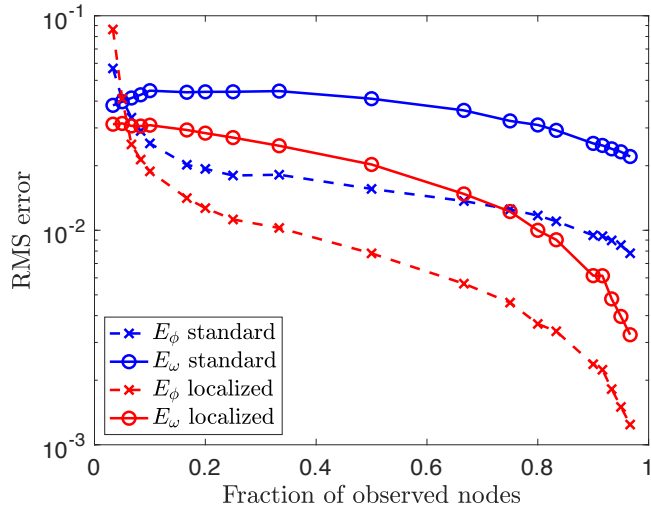


Figure 9: Median RMS errors at $t = 10$ in ϕ (dashed) and ω (solid) for different fractions of observed phases when the EnKF is applied to the Kuramoto model (1) with $N = 60$ nodes and all other parameters the same as in Fig. 1. The median is taken over 100 random realizations of the DA process for each fraction of observed nodes. Results for the standard EnKF are shown in blue, results for the EnKF with network-specific localization are shown in red. Both DA approaches use $M = 2N + 1 = 121$ ensemble members.

a fully synchronized initial condition. Specifically, we continue the simulation shown in Fig. 1 up to time $t = 600$, and use the synchronized end state as the initial condition for a further DA trial. Since we have moved to a co-rotating reference frame, the synchronized state is stationary, and the observed phases are of the form $\phi_i^* + \eta_k$, where ϕ_i^* is the constant phase of the synchronized state and $\eta_k \sim \mathcal{N}(0, 0.02^2)$ is added to create noisy observations. As is shown in Fig. 10, DA with network specific localization is able to improve the estimate of both the phases ϕ_i and the frequencies ω_i , but to a lesser extent than the gain that is made when the transient dynamics is observed (cf. Fig. 8). This is expected because a stationary state carries less information about the dynamics of the system (only an equilibrium solution). We again observe that the standard EnKF does a much worse job of estimating the phases ϕ_i and the frequencies ω_i compared to the localized EnKF.

4.1.3 Random network topologies

We have used the ring topology to illustrate spurious correlations and the benefit of network-specific localization. Our methodology readily extends to general network topologies, and network-specific localization again yields great improvement in estimation accuracy. We show this for random Erdős-Rényi (ER) networks and random modified Barabási-Albert (BA) networks. In ER networks, each pair of nodes is connected with probability p (here we use $p = 0.1$), as such ER networks are highly homogeneous, with a narrow degree distribution around the mean degree $(N - 1)p$. For the BA networks, we use a modified version of the standard generative algorithm, as described in [43]. The algorithm starts with an initial seed network with m_0 nodes, and successive nodes are added iteratively. When a new node is added, n new edges are added to the existing network, with preferential attachment to high degree nodes, where n is drawn uniformly randomly for each new node from $\{m_1, \dots, m_2\}$, with $m_1 \geq 1$ and $m_2 \leq m_0$. In the standard BA algorithm $m_1 = m_2 = m$. Our modified version allows for nodes with smaller degrees, including leaf nodes with degree 1 provided $m_1 = 1$. The BA networks are “scale-free”, having a power law degree distribution and mean degree $m_1 + m_2$. Here we use

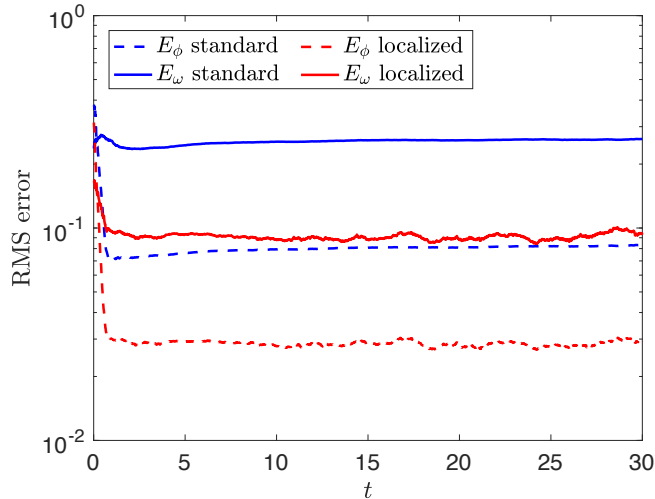


Figure 10: RMS errors in ϕ (dashed) and ω (solid) for DA applied to the Kuramoto model (1) with a fully synchronized initial condition, and with 35 out of $N = 50$ phases observed. Results are shown for the standard (blue) and localized ((23) using $\lambda = 0.46$) (red) EnKF. The Kuramoto model parameters are as in Fig. 1.

$m_1 = 1$, $m_2 = 5$, and an initial seed network with $m_0 = 5$ nodes.

For our network-specific localization, we use the same localization matrix \mathcal{L} defined by (22) and (23) using the positive semi-definite matrix exponential $\mathcal{E} = \exp(\lambda A)$. The value of the tunable parameter λ is determined as described in Section 3.3.

To show the improvement that is gained by employing localization, we consider 500 realizations of the Kuramoto model with ER network topologies and 500 realizations of the Kuramoto model with BA network topologies. All realizations have $N = 50$ nodes and random natural frequencies ω_i drawn from $g(\omega) \sim \mathcal{N}(0, 0.1)$. For each realization we run the EnKF with 35 out of 50 random phases observed, both with and without localization (all other parameters such as the initial ensemble are the same to allow direct comparison). We record the RMS errors in both the phases ϕ_i and the frequencies ω_i at time $t = 10$ (which is the typical synchronization time for such a network with coupling strength $\kappa = 10$, cf. Fig. 1). The results are collected in Fig. 11, which shows the RMS error of the standard EnKF versus that of the localized EnKF for each of the realizations (red crosses for ER networks and black pluses for BA networks) for (a) ϕ , and (b) ω . Data points that fall below the black reference line are those for which the localized EnKF performed better (less error). Fig. 11(a) shows that the localized EnKF produced a better approximation for the phases ϕ_i for 99.2% (496/500) of the ER networks and 95.6% (478/500) of the BA networks. Fig. 11(b) shows that the localized EnKF produced a better prediction for the natural frequencies ω_i for every ER network, and all except one BA network (99.8%). The median reduction in the error when using the localized EnKF compared to the standard EnKF is 61.0% for ϕ_i and 59.8% for ω_i in ER networks, and 53.9% for ϕ_i and 52.8% for ω_i in BA networks. It is clear that incorporating localization yields a great improvement in the estimation accuracy of DA for complex network topologies as well as the ring topology.

4.2 Data assimilation for a network of theta neurons with a ring-like topology

We now apply our DA approach to a network of theta neurons (2), in which synchronization does not generally occur.

As for the Kuramoto model, our task is to estimate all the phases ϕ_i and all the intrinsic

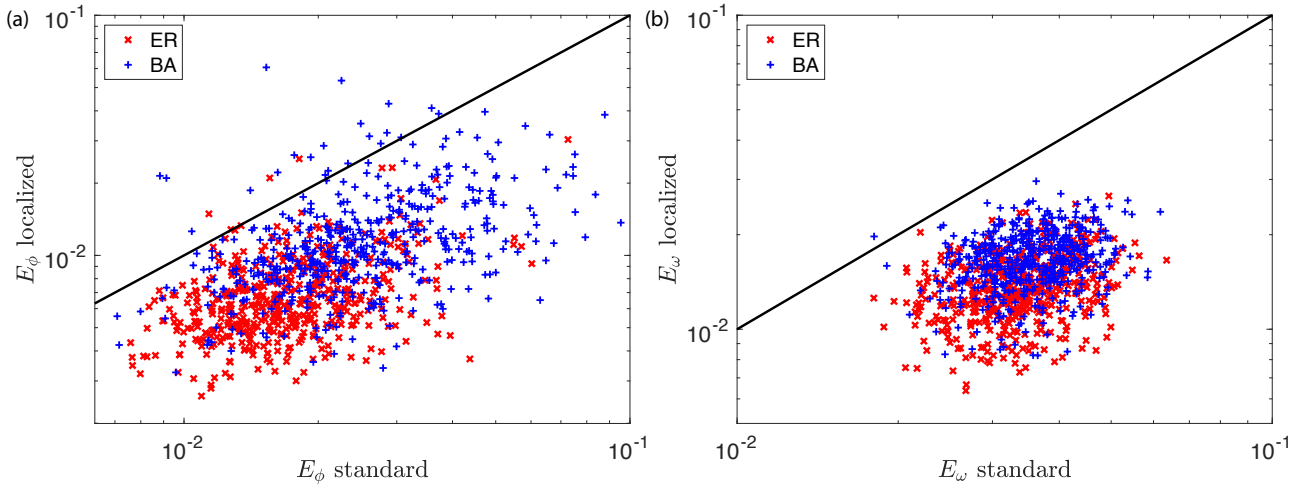


Figure 11: RMS errors at $t = 10$ in (a) ϕ , and (b) ω for DA applied to the Kuramoto model (1) with 35 out of $N = 50$ phases observed. Results are shown for 500 ER network topologies (red crosses) and 500 BA network topologies (blue pluses). All other parameters are as in Fig. 1. Errors using the standard EnKF are shown versus errors using the EnKF with network-specific localization (22) and (23) with λ obtained from (27). The black reference lines show “standard EnKF error” = “localized EnKF error”.

firing parameters ζ_i when only a subset of the phases are observed.

For the connectivity matrix B , we consider a ring topology, such that nodes are positively coupled with $B_{ij} = 1$ if they are within a coupling radius $r = 3$. We also include negative (inhibitory) long-range coupling, such that $B_{ij} = -0.4$ for the three furthest nodes from each node. All other entries of B are zero. This connectivity matrix produces the “bump state” shown in Fig. 2. Similar to the Kuramoto model, correlation matrices for large ensembles reflect the underlying network connectivity. The localization matrix (23) is chosen, with $A_{ij} = |B_{ij}|$ since B has negative entries. We use $\lambda = 0.46$, as determined in Section 3.3 for a ring topology with coupling radius $r = 3$.

We find that localization again significantly improves the estimation capability of the EnKF, and yields accurate estimates for both the ϕ_i and ζ_i when only 35 out of 50 phases are observed. The RMS errors in ϕ_i (dashed) and ζ_i (solid) are shown in Fig. 12(a) for the standard (blue) and localized (red) EnKF. By time $t = 30$, localization has reduced the RMS errors in both the ϕ_i and ζ_i by more than a factor of 10. The relative errors at time $t = 30$ are shown in Fig. 12(b,c). The errors clearly show excellent performance of the EnKF approach with localization. Comparing the median errors (horizontal lines in Fig. 12(b,c)), localization yields more than a 100-fold decrease in error compared to the standard EnKF. As with the Kuramoto model, there is greater discrepancy for the unobserved nodes (open circles/triangles) compared to the observed nodes (filled circles/triangles). For the quiescent, approximately stationary, nodes in the bump state ($i \in [30, 40]$), DA performs slightly worse. This is analogous to the problem of redundant observations in synchronization, though the persistent small fluctuations that occur in the theta neuron model allow for better approximation than a purely stationary synchronized state.

Fig. 13 shows that, as expected, when the fraction of observed phases increases, the estimation accuracy of both the standard and localized EnKF increases. However, the EnKF with localization allows for a much smaller number of observed phases to achieve the same estimation accuracy compared to the standard EnKF. For example, to achieve the same RMS errors as the standard EnKF with 90% of the phases observed, one only needs to observe 20% of the phases using the localized EnKF.

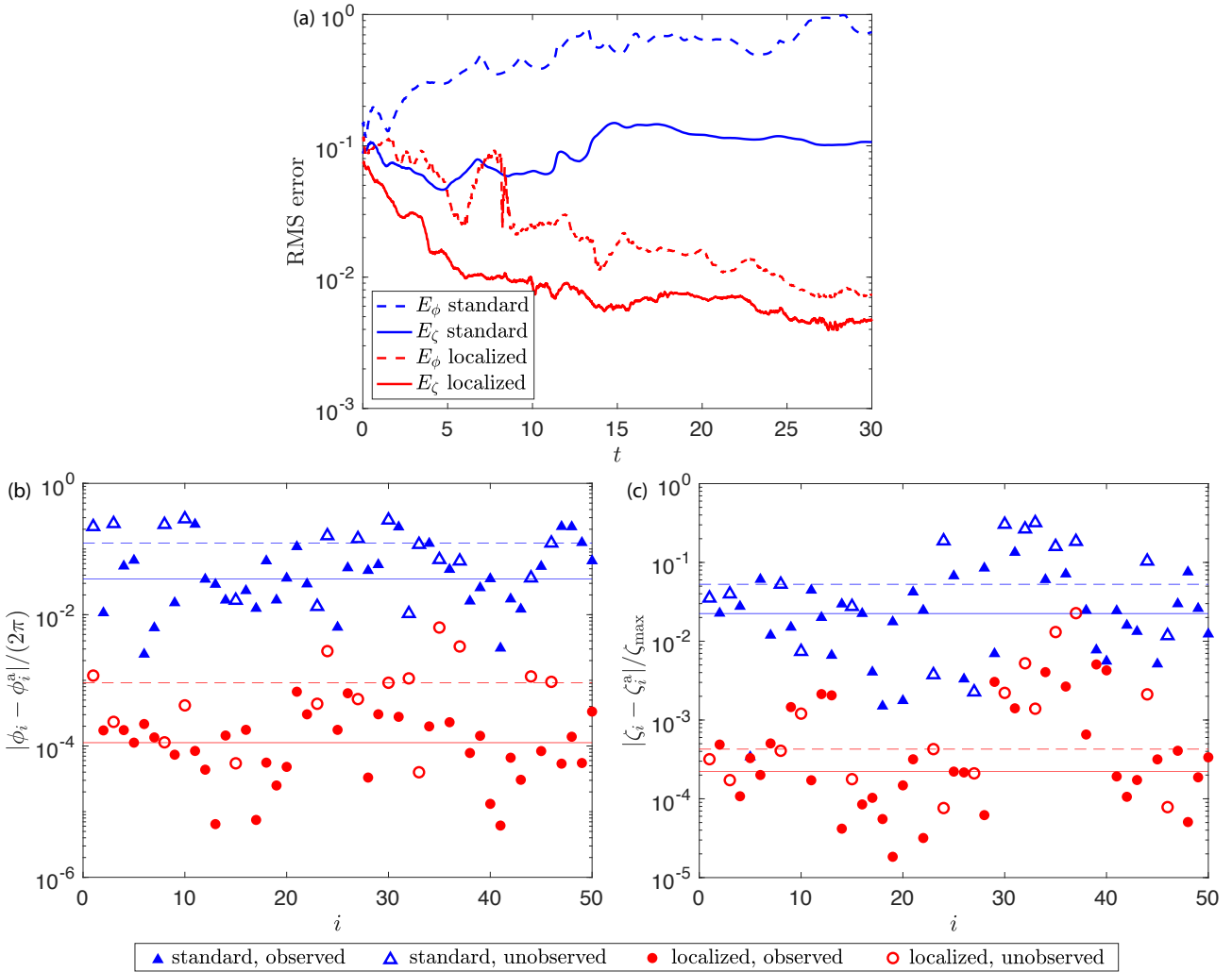


Figure 12: (a) RMS errors in ϕ (dashed) and ζ (solid) for DA applied to a theta neuron network (2) with 35 out of $N = 50$ phases observed. Results are shown for the standard (blue) and localized ((23) using $\lambda = 0.46$) (red) EnKF. (b), (c) Relative errors in ϕ_i and ζ_i , respectively, at final time $t = 30$ for the standard (blue triangles) and localized (red circles) EnKF. Filled symbols indicate observed nodes, and open symbols indicate unobserved nodes. Median errors are shown as horizontal lines; blue for standard, red for localized, solid for observed, dashed for unobserved. The theta neuron model parameters are as in Fig. 2.

DA performs better with overall smaller RMS errors for the theta neuron model (2) than for the Kuramoto model (1), because its dynamics is irregular, and, thus, DA does not suffer from the data degeneracy issue that arises due to synchronization.

5 Conclusion

Data assimilation via the Ensemble Kalman Filter with network-specific localization and state space augmentation (and other minor modifications to account for periodicity of phase variables) can accurately determine both the phases and unknown model parameters in networks of coupled oscillators when only a subset of the phases are observed. Our novel localization approach utilizes the matrix exponential of the network's adjacency matrix, which encodes the connectivity between nodes. We have demonstrated the efficacy of our method for the Kuramoto model that exhibits synchronization, and networks of theta neurons which do not

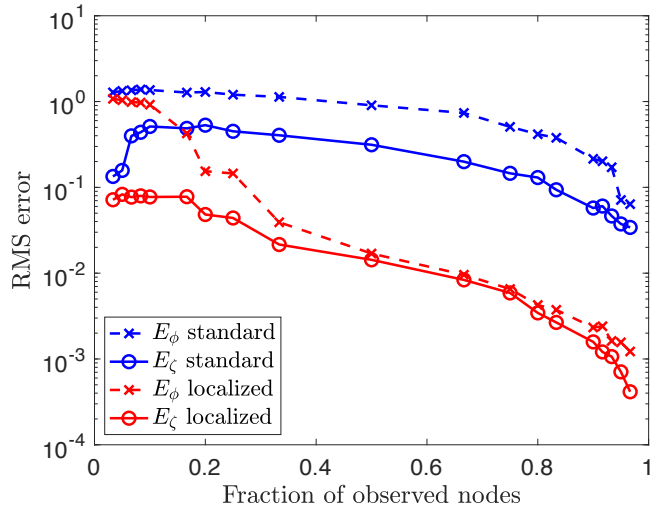


Figure 13: Median RMS errors at $t = 30$ in ϕ (dashed) and ζ (solid) for different fractions of observed phases when the EnKF is applied to the theta neuron model (2) with $N = 60$ nodes and all other parameters the same as in Fig. 2. The median is taken over 100 random realizations of the DA process for each fraction of observed phases. Results for the standard EnKF are shown in blue, results for the EnKF with network-specific localization are shown in red. Both DA approaches use $M = 2N + 1 = 121$ ensemble members.

exhibit synchronization. In both examples, data assimilation yields excellent approximations that closely agree with the truth.

We have considered random subsets for the observed nodes, but it is likely that there are optimal sets of nodes that should be observed. Real-world applications such as the power grid will also have physical limitations on which nodes can be observed. More work is needed to determine an optimal choice of observed nodes.

We have focused on using DA to learn the unknown intrinsic parameters for each oscillator. Future work should investigate whether DA with partial observations can be used to determine unknown coupling functions (estimating Fourier coefficients) or unknown network connectivity matrices [44–49]. Determining the network structure is challenging since there is a large number of unknowns, and our localization method requires an *a priori* known network structure. However, we believe that if the network topology is known reasonably well, e.g., it is known where power lines are in the power grid, but the non-zero weights of the adjacency matrix are not known, then localization can still be performed and the filter will converge.

Our novel localization method is specific to dynamics on networks, but not necessarily to coupled oscillators. We expect our localization approach to also improve DA when applied to other types of dynamics on networks, such as spreading processes (e.g., contagions) [50].

Acknowledgements

We wish to acknowledge support from the Australian Research Council, Grant No. DP180101991, and from the Marsden Fund of the Royal Society of New Zealand, managed by Royal Society Te Apārangi, Project ID 23-UOA-152.

References

- [1] Bick C, Goodfellow M, Laing CR, Martens EA. 2020 Understanding the dynamics of biological and neural oscillator networks through exact mean-field reductions: a review. *The Journal of Mathematical Neuroscience* **10**, 1–43.

- [2] Montbrió E, Pazó D, Roxin A. 2015 Macroscopic description for networks of spiking neurons. *Phys. Rev. X* **5**, 021028. (10.1103/PhysRevX.5.021028)
- [3] Schmidt H, Avitabile D. 2020 Bumps and oscillons in networks of spiking neurons. *Chaos: An Interdisciplinary Journal of Nonlinear Science* **30**, 033133. (10.1063/1.5135579)
- [4] Machowski J, Bialek JW, Bumby J. 2011 *Power system dynamics: stability and control*. John Wiley & Sons.
- [5] Nishikawa T, Motter AE. 2015 Comparative analysis of existing models for power-grid synchronization. *New J. Phys.* **17**. (10.1088/1367-2630/17/1/015012)
- [6] Filatrella G, Nielsen AH, Pedersen NF. 2008 Analysis of a power grid using a Kuramoto-like model. *Eur. Phys. J. B* **61**.
- [7] Schäfer B, Yalcin GC. 2019 Dynamical modeling of cascading failures in the Turkish power grid. *Chaos* **29**. (10.1063/1.5110974)
- [8] Evensen G. 1994 Sequential data assimilation with a nonlinear quasi-geostrophic model using Monte Carlo methods to forecast error statistics. *J. Geophys. Res.-Oceans* **99**.
- [9] Houtekamer PL, Mitchell HL. 1998 Data assimilation using an ensemble Kalman filter technique. *Mon. Weather Rev.* **126**.
- [10] Jazwinski AH. 2007 *Stochastic processes and filtering theory*. Courier Corporation.
- [11] Evensen G. 2009a *Data assimilation: The ensemble Kalman filter* vol. 2. Springer.
- [12] Evensen G. 2009b The ensemble Kalman filter for combined state and parameter estimation. *IEEE Contr. Syst. Mag.* **29**.
- [13] Reich S, Cotter C. 2015 *Probabilistic forecasting and Bayesian data assimilation*. Cambridge University Press.
- [14] Law K, Stuart A, Zygalakis K. 2015 *Data assimilation: A mathematical introduction*. New York: Springer-Verlag.
- [15] Carrillo J, Hoffmann F, Stuart A, Vaes U. 2024 The mean field ensemble Kalman filter: Near-Gaussian setting. *arXiv preprint arXiv:2212.13239*.
- [16] Forero-Ortiz E, Tirabassi G, Masoller C, Pons AJ. 2021 Inferring the connectivity of coupled chaotic oscillators using Kalman filtering. *Scientific Reports* **11**, 22376. (10.1038/s41598-021-01444-7)
- [17] Aristides RP, Pons AJ, Cerdeira HA, Masoller C, Tirabassi G. 2023 Parameter and coupling estimation in small networks of Izhikevich's neurons. *Chaos* **33**, 043123. (10.1063/5.0144499)
- [18] Houtekamer PL, Mitchell HL. 2001 A sequential ensemble Kalman filter for atmospheric data assimilation. *Monthly Weather Review* **129**, 123 – 137. (10.1175/1520-0493(2001)129;0123:ASEKFF;2.0.CO;2)
- [19] Al-Ghaffas O, Chen J, Sanz-Alonso D, Waniorek N. 2024 Covariance operator estimation: Sparsity, lengthscale, and ensemble Kalman filters. *arXiv preprint arXiv: 2310.16933*.

- [20] Panaggio MJ, Ciocanel MV, Lazarus L, Topaz CM, Xu B. 2019 Model reconstruction from temporal data for coupled oscillator networks. *Chaos* **29**. (10.1063/1.5120784)
- [21] Shandilya SG, Timme M. 2011 Inferring network topology from complex dynamics. *New J. Phys.* **13**. (10.1088/1367-2630/13/1/013004)
- [22] Pikovsky A. 2018 Reconstruction of a random phase dynamics network from observations. *Phys. Lett. A* **382**.
- [23] Owens K, Kutz JN. 2023 Data-driven discovery of governing equations for coarse-grained heterogeneous network dynamics. *SIAM Journal on Applied Dynamical Systems* **22**, 2601–2623.
- [24] Kuramoto Y. 1984 *Chemical Oscillations, Waves, and Turbulence*. Berlin: Springer-Verlag. (10.1007/978-3-642-69689-3)
- [25] Strogatz SH. 2000 From Kuramoto to Crawford: Exploring the onset of synchronization in populations of coupled oscillators. *Physica D* **143**. (10.1016/S0167-2789(00)00094-4)
- [26] Pikovsky A, Rosenblum M, Kurths J. 2001 *Synchronization: A Universal Concept in Non-linear Sciences*. Cambridge: Cambridge University Press.
- [27] Acebrón JA, Bonilla LL, Pérez Vicente CJ, Ritort F, Spigler R. 2005 The Kuramoto model: A simple paradigm for synchronization phenomena. *Rev. Mod. Phys.* **77**. (10.1103/RevModPhys.77.137)
- [28] Osipov GV, Kurths J, Zhou C. 2007 *Synchronization in Oscillatory Networks*. Berlin: Springer. (10.1007/978-3-540-71269-5)
- [29] Arenas A, Diaz-Guilera A, Kurths J, Moreno Y, Zhou C. 2008 Synchronization in complex networks. *Phys. Rep.* **469**. (10.1016/j.physrep.2008.09.002)
- [30] Dörfler F, Bullo F. 2014 Synchronization in complex networks of phase oscillators: A survey. *Automatica* **50**.
- [31] Rodrigues FA, Peron TKD, Ji P, Kurths J. 2016 The Kuramoto model in complex networks. *Phys. Rep.* **610**.
- [32] Laing CR. 2014 Derivation of a neural field model from a network of theta neurons. *Phys. Rev. E* **90**, 010901. (10.1103/PhysRevE.90.010901)
- [33] Laing CR. 2018 The dynamics of networks of identical theta neurons. *The Journal of Mathematical Neuroscience* **8**, 1–24.
- [34] Laing CR, Omel’chenko O. 2020 Moving bumps in theta neuron networks. *Chaos: An Interdisciplinary Journal of Nonlinear Science* **30**, 043117. (10.1063/1.5143261)
- [35] Omel’chenko O, Laing CR. 2022 Collective states in a ring network of theta neurons. *Proceedings of the Royal Society A: Mathematical, Physical and Engineering Sciences* **478**, 20210817. (10.1098/rspa.2021.0817)
- [36] Bressloff PC. 2012 Spatiotemporal dynamics of continuum neural fields. *Journal of Physics A: Mathematical and Theoretical* **45**, 033001. (10.1088/1751-8113/45/3/033001)

- [37] Wimmer K, Nykamp DQ, Constantinidis C, Compte A. 2014 Bump attractor dynamics in prefrontal cortex explains behavioral precision in spatial working memory. *Nature Neuroscience* **17**, 431–439.
- [38] Anderson JL. 2001 An ensemble adjustment Kalman filter for data assimilation. *Monthly Weather Review* **129**, 2884 – 2903. (10.1175/1520-0493(2001)129;2884:AEAKFF;2.0.CO;2)
- [39] Burgers G, van Leeuwen PJ, Evensen G. 1998 Analysis scheme in the ensemble Kalman filter. *Monthly Weather Review* **126**, 1719–1724. (10.1175/1520-0493(1998)126;1719:ASITEK;2.0.CO;2)
- [40] Law K, Stuart A, Zygalakis K. 2015 *Data assimilation: A mathematical introduction*. New York: Springer-Verlag.
- [41] Anderson JL, Anderson SL. 1999 A Monte Carlo implementation of the nonlinear filtering problem to produce ensemble assimilations and forecasts. *Monthly Weather Review* **127**, 2741 – 2758. (10.1175/1520-0493(1999)127;2741:AMCIOT;2.0.CO;2)
- [42] Gaspari G, Cohn SE. 1999 Construction of correlation functions in two and three dimensions. *Quarterly Journal of the Royal Meteorological Society* **125**, 723–757. (<https://doi.org/10.1002/qj.49712555417>)
- [43] Smith LD, Gottwald GA. 2021 Mesoscopic model reduction for the collective dynamics of sparse coupled oscillator networks. *Chaos* **31**. 073116 (10.1063/5.0053916)
- [44] Peixoto TP. 2018 Reconstructing networks with unknown and heterogeneous errors. *Phys. Rev. X* **8**, 041011. (10.1103/PhysRevX.8.041011)
- [45] Peixoto TP. 2019 Network reconstruction and community detection from dynamics. *Phys. Rev. Lett.* **123**, 128301. (10.1103/PhysRevLett.123.128301)
- [46] Tyloo M, Delabays R, Jacquod P. 2021 Reconstructing network structures from partial measurements. *Chaos: An Interdisciplinary Journal of Nonlinear Science* **31**, 103117. (10.1063/5.0058739)
- [47] Deng W, Yang C, Huang K, Wu W. 2022 A two-stage reconstruction method for complex networked system with hidden nodes. *Chaos: An Interdisciplinary Journal of Nonlinear Science* **32**, 053105. (10.1063/5.0087740)
- [48] Chen M, Zhang Y, Zhang Z, Du L, Wang S, Zhang J. 2022 Inferring network structure with unobservable nodes from time series data. *Chaos: An Interdisciplinary Journal of Nonlinear Science* **32**, 013126. (10.1063/5.0076521)
- [49] Gaskin T, Pavliotis GA, Girolami M. 2023 Inferring networks from time series: a neural approach. *arXiv preprint arXiv:2303.18059*.
- [50] De Domenico M, Granell C, Porter MA, Arenas A. 2016 The physics of spreading processes in multilayer networks. *Nature Physics* **12**, 901–906.